RSC Advances

PAPER

View Article Online
View Journal | View Issue

Cite this: *RSC Adv.*, 2024, **14**, 20646

Performance and mechanism of U(VI) removal from solution by humic acid-coated Fe_3O_4 nanoparticle-modified biochar from filamentous green algae†

Mingyang Shen,[a] Weisheng Dai,[bc] Muqing Qiu *[b] and Baowei Hu [b]

Received 9th May 2024
Accepted 16th June 2024

DOI: 10.1039/d4ra03421j

rsc.li/rsc-advances

The adsorbent material humic acid-coated Fe_3O_4 nanoparticle-modified biochar from filamentous green algae was fabricated by introducing the composites of humic acid-coated Fe_3O_4 nanoparticles onto biochar from filamentous green algae using the co-precipitation method. Then, the removal of U(VI) from solution by humic acid–Fe_3O_4/BC was carried out through batch experiments. The results of the characterization showed that the reaction conditions had an important influence on U(VI) removal by humic acid–Fe_3O_4/BC. The pseudo-second-order kinetic model and Langmuir model better illustrate the adsorption process of U(VI) on the surface of humic acid–Fe_3O_4/BC. The adsorption processes were dominated by chemisorption and monolayer adsorption. The maximum adsorption capacity of U(VI) by humic acid–Fe_3O_4/BC could be calculated, and it could reach 555.56 mg g^{-1}. The probable mechanisms of U(VI) removal by humic acid–Fe_3O_4/BC were reduction reaction, inner-sphere surface complexation and electrostatic adsorption. The high stability and reusability of humic acid–Fe_3O_4/BC made it more promising in U(VI) removal applications.

1 Introduction

With the gradual warming of the global climate and the demand for increasing energy, many countries have started to increase their investment in nuclear energy to meet the increasing energy needs of people and reduce the pressure on greenhouse gas emissions.[1,2] However, it also raises other serious issues that cannot be ignored. For instance, with the development of mining and the long-term operation of nuclear energy and nuclear fuel cycle facilities, an increasing number of radioactive nuclides is released into the environment.[3,4] The large amount of uranium-contaminated wastewater from uranium tailings and nuclear fuel treatment waste has seriously affected groundwater, surface water, and soil around the world.[5,6] Uranium(VI) is considered one of the most common radioactive nuclides in wastewater and poses a potential threat to human health and the environment due to its radioactivity and toxicity to humans.[7] It can accumulate in organs and bones, enhancing the possibility of damage to DNA and the reproductive system.[8,9] Therefore, how to efficiently treat uranium containing wastewater will be of great significance for the quality of human life and environmental protection.[10,11]

For the past few years, a large number of technologies have been currently applied for the treatment of U(VI) from wastewater, such as chemical precipitation, electrochemical process, adsorption, photocatalysis, membrane separation, solvent extraction, and ion exchange.[12–18] Among these technologies, adsorption technology is believed to be the most effective technology for U(VI) removal because of its high efficiency, economic benefit, easy operation, and lack of generation of environmentally toxic byproducts.[19–21] Moreover, the long-term use of adsorbents implies a complicated preparation process, high manufacturing costs, energy-intensive detachability, and a negative environmental influence. Thus, this highly limits their applicability.[22] Therefore, the preparation of high-performance adsorption materials has been a popular research topic for the high-efficiency elimination of U(VI)-containing wastewater.[23]

In recent years, biochar (BC) has attracted the attention of a large number of scholars owing to its characteristics of low cost, sustainability, diverse oxygen-containing functional groups, high specific surface area and stable porous structure. It is known as a by-product of hydrothermal carbonization and pyrolysis under oxygen-limited reaction conditions.[24] Therefore, biochar can be applied for environmental pollutant removal. Biochar can be derived from various raw waste materials, such as rice husk, waste sludge, cellulose, waste paper, crop straw, fruit peels, waste wood, and poultry manure.[25–28] They can be recycled as biomass resources. In the past few decades, people have struggled with the abundance of algae. A large number of algae are produced in the lake. If excessive algae in the lake are

[a]College of Life Sciences, Nanjing Agricultural University, 210095, P. R. China
[b]College of Life and Environmental Science, Shaoxing University, 312000, P. R. China. E-mail: qiumuqing@usx.edu.cn
[c]Shaoxing Raw Water Group Co., LTD., Shaoxing, 312000, P. R. China

† Electronic supplementary information (ESI) available. See DOI: https://doi.org/10.1039/d4ra03421j

not cleaned up promptly, it may produce hydrogen sulfide, algal toxins, and other toxic and harmful substances. This poses a huge danger to the environment. Because algae are also biological resources, it is necessary to utilize them as biomass resources. In recent years, many researchers have carried out several studies on the preparation of biochar from algae. Biochar derived from wakame, natural algae, and macro-algae also has strong adsorption capacity. It can remove various environmental pollutants.[29–31]

To improve the adsorption ability and maximize the recycling of biochar from aqueous solutions, magnetic biochar composites have been widely elaborated in detail. A large number of reports have shown that magnetic biochar greatly improved the adsorption capacity and achieved the purpose of recycling.[32,33] The U(VI) ions in an aqueous solution can be adsorbed onto the surface of iron oxide nanoparticles.[34,35] Additionally, they can be quickly recovered through magnetic separation.[36–38] Therefore, microscale magnetite and magnetite nanoparticles (Fe_3O_4 nanoparticles) have attracted significant attention owing to their application in engineered adsorption processes. However, Fe_3O_4 nanoparticles are easy to aggregate.[39] This shortcoming affects their elimination efficiency. Thus, it also restricts their large-scale engineering application in environmental remediation. Therefore, the surface modification of Fe_3O_4 nanoparticles can reduce particle aggregation and improve reaction performance.[40]

Humic acid (HA) is ubiquitous in surface water, groundwater, and soil systems.[37] It contains abundant sulfhydryl functional groups, carboxylic functional groups, and phenolic functional groups. Therefore, it can be used as an inexpensive and simple means of coating Fe_3O_4 nanoparticles to reduce the aggregation reaction of Fe_3O_4 nanoparticles through electrostatic repulsive forces between HA and Fe_3O_4 nanoparticles. Additionally, it can form strong bonds with environmental pollutants through its abundant sulfhydryl functional groups, carboxylic functional groups, and phenolic functional groups. Therefore, the composites of HA coatings on Fe_3O_4 nanoparticles can lead to the highly effective adsorption of environmental pollution in a solution.[41] Related studies on the preparation and application of HA-coated Fe_3O_4 nanoparticles have been reported.[42] Although some studies have tested U(VI) removal from solution by HA-coated Fe_3O_4 nanoparticles, few studies have been conducted on U(VI) removal from solution by HA-coated Fe_3O_4 nanoparticle-modified biochar from algae.[43]

In this study, biochar was derived from filamentous green algae. Then, humic acid-coated Fe_3O_4 nanoparticles modified biochar (HA–Fe_3O_4/BC) were fabricated by introducing the composites of humic acid-coated Fe_3O_4 nanoparticles onto the biochar with the co-precipitation method. Then, the performance of U(VI) removal from the solution by HA–Fe_3O_4/BC was carried out through batch experiments. The main objectives of this work were to (1) elaborate the characteristics of HA–Fe_3O_4/BC; (2) survey the interfacial adsorption behavior of U(VI) removal by HA–Fe_3O_4/BC and the effects of the related reaction conditions; (3) elucidate the removal mechanism of U(VI) removal by HA–Fe_3O_4/BC through XPS analyses; and (4) assess the chemical stability of U(VI) removal by HA–Fe_3O_4/BC by recycling adsorption experiments.

2 Materials and method

2.1 Materials

Chemical reagents and preparation of BC are shown in ESI.†

2.2 Preparation of HA–Fe_3O_4/BC

HA–Fe_3O_4/BC was synthesized according to a previous study using the co-precipitation method.[33,44] Briefly, 2.78 g of $FeSO_4 \cdot 7H_2O$ and 1.62 g of $FeCl_3$ were added to 250 mL of the conical flask with a stopper and dissolved with 100 mL of deoxygenated water. The

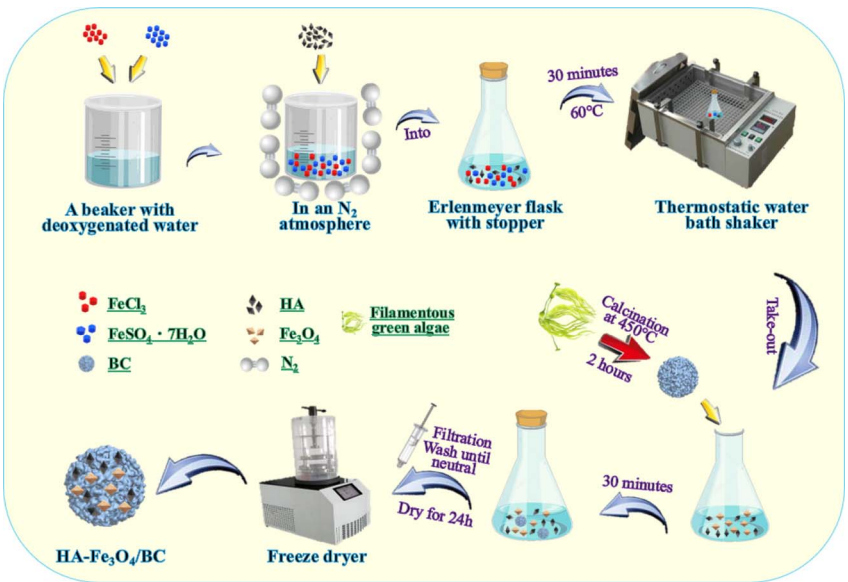

Fig. 1 Synthesis procedure of HA–Fe_3O_4/BC composites.

deionized water was deoxygenated for 10 min by heating to a temperature of 100 °C. Then, 1.0 g of HA was rapidly added to the mixture solution under a N_2 atmosphere. Next, they were stirred and placed at 60 °C for 30 min under a thermostat water bath. Subsequently, 5.0 g of biochar from the filamentous green algae was added to the mixture solution. After 30 min, the precipitated composites were collected, filtered, washed with deionized water until neutral, and freeze-dried for 24 h. Finally, the composites of HA–Fe_3O_4/BC were obtained. The synthesis procedure of HA–Fe_3O_4/BC composites is displayed in Fig. 1.

2.3 Adsorption experiments

The adsorption of U(VI) removal by HA–Fe_3O_4/BC was tested through a series of batch experiments. 10 mg of HA–Fe_3O_4/BC was added into a 250 mL Erlenmeyer flask. Then, 100 mL of U(VI) solution was put into the Erlenmeyer flask. Then, it was placed in a water bath shaker. The reaction conditions, such as pH in solution, reaction time, reaction temperature and the initial concentration of U(VI), could be fixed. After the reaction reached equilibrium, the adsorption experiment was completed. The concentration of U(VI) in the solution was measured by Arsenazo-III colorimetry using a UV-vis spectrophotometer at 650 nm.[37] Each adsorption experiment was tested three times under the same reaction conditions. The results are taken as the arithmetic mean.

2.4 Characterization

Samples were characterized by technologies of SEM, TEM, FT-IR, XRD and XPS. The detailed information is shown in ESI.†

3 Results and discussion

3.1 Characterization of BC and HA–Fe_3O_4/BC

The results of the SEM images were used to characterize the surface morphology of BC (the original biochar) and HA–Fe_3O_4/BC (the modified biochar with the composites of HA and Fe_3O_4 nanoparticles). The SEM images of BC and HA–Fe_3O_4/BC are displayed in Fig. 2.

Comparing the surface morphology of BC (Fig. 2A) and HA–Fe_3O_4/BC (Fig. 2B), the difference in surface morphology could be observed. After modification with the composites of the HA and Fe_3O_4 nanoparticles, the basic surface structure of biochar was not destroyed compared to the unmodified biochar. From Fig. 2A, it could be observed that BC was an irregular and smooth surface. However, the surface of HA–Fe_3O_4/BC became rougher and had an irregular surface structure. Some flocculent particles appeared on the surface of HA–Fe_3O_4/BC. The appearance of these flocculent particles indicated that they might be the composites of HA and Fe_3O_4 nanoparticles. To further verify these flocculent particles, the characterization of BC and HA–Fe_3O_4/BC was determined by these technologies of FT-IR, XRD and XPS. The related results are displayed in Fig. 3.

The surface functional groups of BC and HA–Fe_3O_4/BC were compared through the FT-IR spectra (Fig. 3A). For BC, the peak at 3404 cm^{-1} appeared, and it was ascribed to the group of –O–H stretching vibration. This indicates that hydroxyl groups on the surface of BC were observed.[45] The two peaks at 1610 cm^{-1} and 1383 cm^{-1} of BC represented –C=C– and $-CH_3$ or $-CH_3$ functional groups, respectively.[46] The peak at 1060 cm^{-1} appeared, and it was ascribed to the group of –C–O–C– stretching vibration.[47] For HA–Fe_3O_4/BC, the peaks at 3410 cm^{-1}, 1608 cm^{-1}, 1381 cm^{-1}, and 1053 cm^{-1} appeared, and they represent –O–H stretching vibration, –C=C– stretching vibration, $-CH_3$ stretching vibration and –C–O–C– stretching vibration, respectively. Additionally, the peak of HA–Fe_3O_4/BC at 467 cm^{-1} was assigned to the stretching vibration of Fe–O functional group.[48]

The crystal phase and structural information of BC and HA–Fe_3O_4/BC were analyzed according to the results of the XRD pattern. The XRD patterns of BC and HA–Fe_3O_4/BC are displayed in Fig. 3B. As shown in Fig. 3B, six reflections are at 2θ = 74.06, 66.38, 58.84, 50.12, 40.52 and 28.31°. PDF card no. 96-900-5840 indexed to the magnetite lattice planes are (220), (311), (400), (511), and (440).[49] They presented strong signals of Fe_3O_4 nanoparticles. Therefore, they also indicated the successful coating of Fe_3O_4 nanoparticles onto BC.

The changes in functional groups on BC and HA–Fe_3O_4/BC were elaborated through the results of XPS spectra (Fig. 3C and D). From Fig. 3C, the two wide photoelectron lines at the binding energies at 284.06 and 531.06 eV appeared, and they were attributed to C 1s and O 1s, respectively. The main element components of HA–Fe_3O_4/BC composites were C (76.84% (wt%)) and O (23.16% (wt%)). As shown in Fig. 3D, the three wide photoelectron lines at the binding energies at 284.06, 531.06 and 710.28 eV

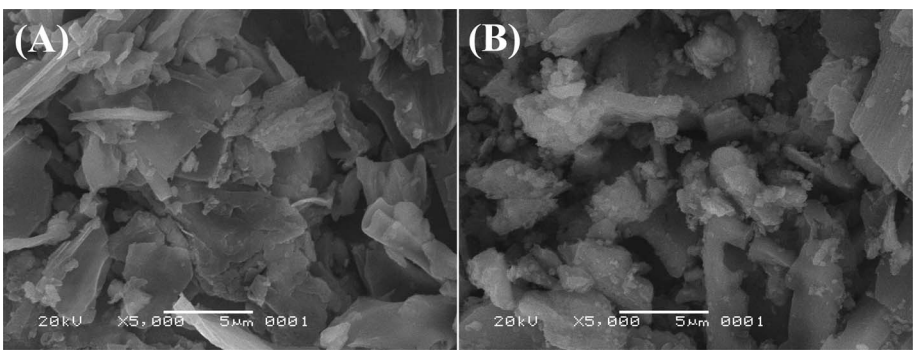

Fig. 2 SEM images of BC (A) and HA–Fe_3O_4/BC (B).

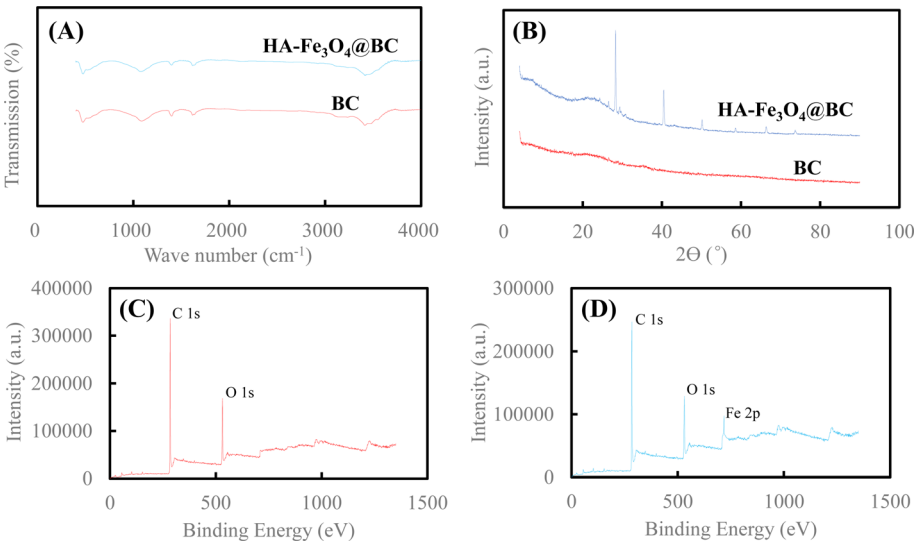

Fig. 3 (A) FT-IR spectra of BC and HA–Fe_3O_4/BC, (B) XRD patterns of BC and HA–Fe_3O_4/BC, (C) XPS spectra of BC and (D) XPS spectra of HA–Fe_3O_4/BC.

appeared, and they were attributed to C 1s, O 1s and Fe 2p, respectively. The main element components of HA–Fe_3O_4/BC composites were C (76.84% (wt%)), O (17.72% (wt%)) and Fe (5.44% (wt%)). The occurrence of the Fe 2p peak (at 710.28 eV) for HA–Fe_3O_4/BC demonstrated the element of Fe loading onto BC. In other words, the composites of HA–Fe_3O_4/BC were successfully fabricated by introducing the composites of humic acid-coated Fe_3O_4 nanoparticles onto the biochar from filamentous green algae using the co-precipitation method.

3.2 Adsorption experiments

3.2.1 Effect of operational parameters. The reaction conditions (such as contact time, initial concentration of U(VI), pH and temperature) were significant factors affecting the adsorption capacity of U(VI) by HA–Fe_3O_4/BC. The effects of operational parameters on U(VI) removal by HA–Fe_3O_4/BC were displayed in Fig. 4.

Fig. 4A illustrates the influence of contact time on U(VI) removal by HA–Fe_3O_4/BC. This adsorption experiment was carried out at different reaction times (t = 5–300 min). The other reaction conditions were as follows: initial concentration of U(VI) was 50 mg L^{-1}, the dosage of HA–Fe_3O_4/BC was 0.3 g L^{-1}, pH in solution was 6.0 and reaction temperature was 298 K. As exhibited in Fig. 4A, the adsorption process could be divided into two stages. In the first adsorption stage, the removal rate of U(VI) by HA–Fe_3O_4/BC increased quickly as the reaction time increased. The adsorption capacity of U(VI) by HA–Fe_3O_4/BC

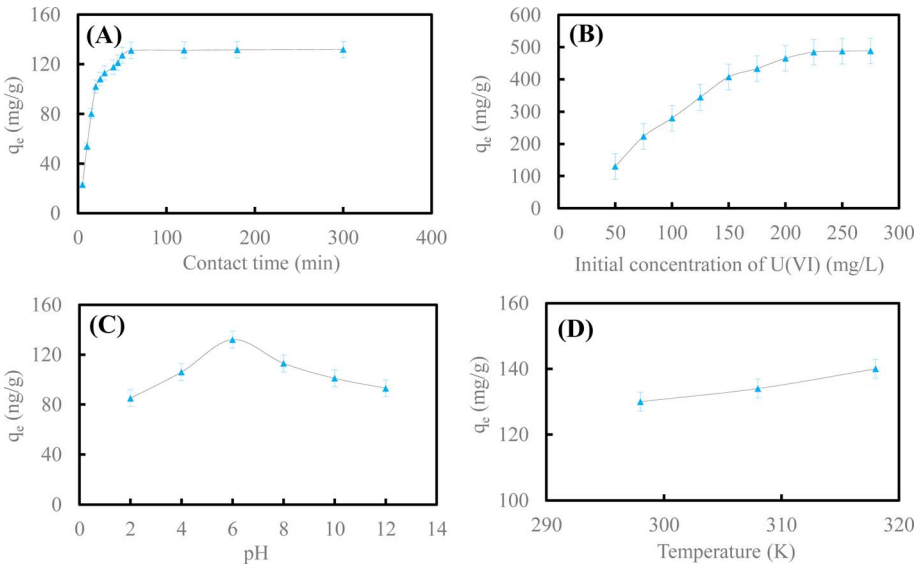

Fig. 4 Effect of contact time (A) and initial concentration of U(VI) (B); pH (C) and reaction temperature (D) on U(VI) removal by HA–Fe_3O_4/BC.

reached 127.2 mg g^{-1} at a reaction time of 60 min. In the second adsorption stage, the removal rate of U(VI) by HA–Fe_3O_4/BC increased slowly and reached equilibrium. At this adsorption stage, the adsorption capacity of U(VI) by HA–Fe_3O_4/BC only increased by 4.56 mg g^{-1}. The removal rate of U(VI) by HA–Fe_3O_4/BC increased slowly. A large number of adsorption sites on the surface of HA–Fe_3O_4/BC appeared at the first adsorption stage. They could be conducive to more U(VI) on the surface of HA–Fe_3O_4/BC. With an increase in reaction time, the adsorption sites on the surface of HA–Fe_3O_4/BC started to decrease gradually. They were slowly covered by U(VI), and the adsorption processes gradually reached equilibrium.[1]

Fig. 4B depicts the influence of the initial concentration of U(VI) on U(VI) removal by HA–Fe_3O_4/BC. The adsorption experiments were carried out at different initial concentrations of U(VI) (C_0 = 50–275 mg L^{-1}). The other reaction conditions were as follows: the dosage of HA–Fe_3O_4/BC was 0.3 g L^{-1}, reaction time was 300 min, pH in solution was 6.0 and reaction temperature was 298 K. As shown in Fig. 4B, the removal capacity of U(VI) by HA–Fe_3O_4/BC increased slowly with the increase in the initial concentration of U(VI) in the solution. This indicated that the initial concentration of U(VI) had an important influence on the removal capacity, and a high initial concentration of U(VI) would improve the removal capacity of U(VI). This is due to the interaction between U(VI) ions from the solution and the adsorbent. When the initial concentration of U(VI) ions from the solution increased, the driving force of the solution mass on the surface of BC and HA–Fe_3O_4/BC increased. Therefore, the adsorption capacity increased with an increase in the initial concentration.

Fig. 4C shows the influence of pH in solution on U(VI) removal by HA–Fe_3O_4/BC. The adsorption experiments were carried out at a different initial pH (pH = 2.0–12.0) adjusted with (1 + 1) H_2SO_4 and 10% NaOH solution. The other reaction conditions were as follows: the dosage of HA–Fe_3O_4/BC was 0.3 g L^{-1}, the reaction time was 300 min, the initial concentration of U(VI) was 50 mg L^{-1} and the reaction temperature was 298 K. As shown in Fig. 4C, the removal capacity of U(VI) by HA–Fe_3O_4/BC increased gradually at pH ranging from 2.0 to 6.0. Then, it started to decrease slowly at pH ranging from 6.0 to 12.0. The species of U(VI) under a different pH in solution had an important influence on the removal capacity of U(VI) by HA–Fe_3O_4/BC. At pH < 4.0, the species of U(VI) in solution were mainly UO_2^{2+}. At pH ranging from 4.0–8.0, the species of U(VI) in solution were $(UO_2)_3(OH)_5^{+}$ and UO_2OH^{+}. At pH > 8.0, the species of U(VI) in solution were $(UO_2)_3(OH)_7^{-}$ and $UO_2(OH)_3^{-}$. Therefore, the positively and negatively charged HA–Fe_3O_4/BC appeared at pH 8.0. The removal capacity of U(VI) was possibly ascribed to the electrostatic interaction between the negative surface charges of HA–Fe_3O_4/BC and the positive species of U(VI) in the solution. The negatively charged surface of HA–Fe_3O_4/BC with abundant binding sites increased as the pH in the solution increased. This result is similar to those of previous studies.[3,50]

Fig. 4D depicts the influence of reaction temperature on U(VI) removal by HA–Fe_3O_4/BC. The adsorption experiments were carried out at different reaction temperatures (T = 298 K, 308 K and 318 K). The other reaction conditions were as follows: the dosage of HA–Fe_3O_4/BC was 0.3 g L^{-1}, the reaction time was 300 min, the initial concentration of U(VI) was 50 mg L^{-1} and the pH in solution was 6.0. As shown in Fig. 4D, the removal capacity of U(VI) by HA–Fe_3O_4/BC increased as the reaction temperature increased. When the reaction temperature rose from 298 K to 318 K, the value of removal capacity increased from 129.16 mg g^{-1} to 141.23 mg g^{-1}. This indicated that the reaction temperature affected the diffusion of U(VI) in the solution. The reaction temperature could increase the rate of mass transfer from the bulk to the boundary layer surrounding the surface of HA–Fe_3O_4/BC.

3.2.2 Adsorption kinetics and adsorption isotherms. To illustrate the adsorption process of U(VI) removal by HA–Fe_3O_4/BC, the adsorption kinetics of U(VI) removal by HA–Fe_3O_4/BC were described using the pseudo-first-order model and pseudo-second-order model. The adsorption isotherms of U(VI) removal by HA–Fe_3O_4/BC were elaborated with the Langmuir and Freundlich models, respectively. They were represented using eqn (1)–(4):[51–54]

$$q_t = q_e(1 - e^{-K_1 t}), \quad (1)$$

$$\frac{t}{q_t} = \frac{1}{K_2 {q_e}^2} + \frac{t}{q_e}, \quad (2)$$

$$q_e = \frac{q_m C_e K_L}{1 + C_e K_L}, \quad (3)$$

$$q_e = K_f {C_e}^{1/n}. \quad (4)$$

According to the data of Fig. 4A and B and eqn (1)–(4), adsorption kinetics and adsorption isotherms of U(VI) removal by HA–Fe_3O_4/BC are displayed in Fig. 5.

As shown in Fig. 5A and B, the pseudo-second-order kinetic model could better illustrate the adsorption process of U(VI) on the surface of HA–Fe_3O_4/BC (R^2 = 0.9952 > 0.7351). The values of pseudo-second-order kinetics were close to the results of the adsorption experiment. This implies that the adsorption processes of U(VI) on the surface of HA–Fe_3O_4/BC were mainly chemisorption.[1] As displayed in Fig. 5C and D, the Langmuir model was more consistent with the adsorption process of U(VI) on the surface of HA–Fe_3O_4/BC than the Freundlich model (R^2 = 0.9831 > 0.6468). This indicates that the adsorption process of U(VI) on the surface of HA–Fe_3O_4/BC was dominated by monolayer adsorption. According to the Langmuir model, the maximum adsorption capacity of U(VI) by HA–Fe_3O_4/BC could be calculated, and it could reach 555.56 mg g^{-1}. Compared with the related reported, HA–Fe_3O_4/BC exhibited excellent adsorption performance of U(VI) removal, low cost and wide source. This indicates that these materials of HA–Fe_3O_4/BC could be widely used in the treatment of U(VI) wastewater.

3.2.3 Possible mechanism. To elaborate on the possible mechanism of U(VI) removal by HA–Fe_3O_4/BC, XPS spectra were examined. The related results of XPS spectra are displayed in Fig. 6.

As shown in Fig. 6A, for HA–Fe_3O_4/BC before the adsorption, the peaks at 283.77, 525.18 and 700.18 eV could be attributed to

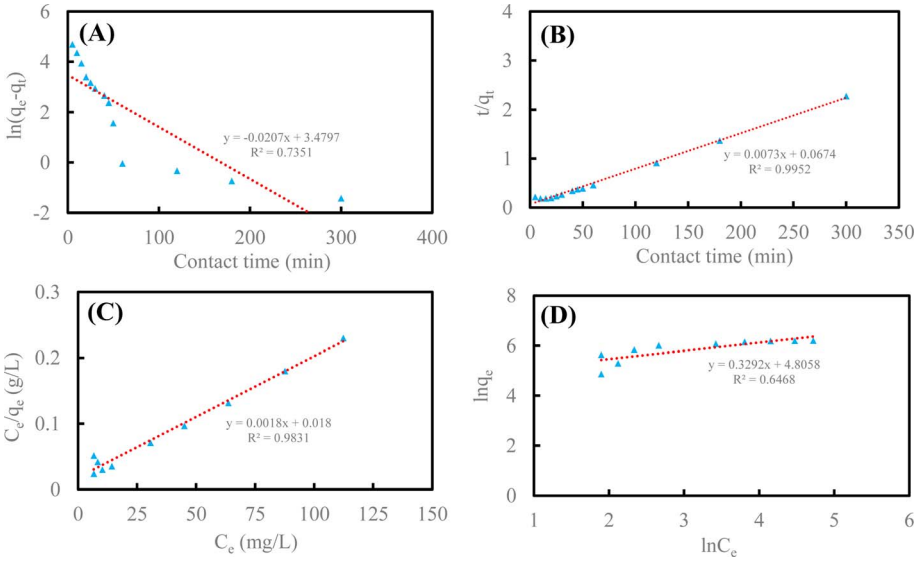

Fig. 5 Adsorption kinetics and adsorption isotherms of U(VI) removal by HA–Fe_3O_4/BC (pseudo-first-order model (A), pseudo-second-order model (B), Langmuir model (C) and Freundlich model (D)).

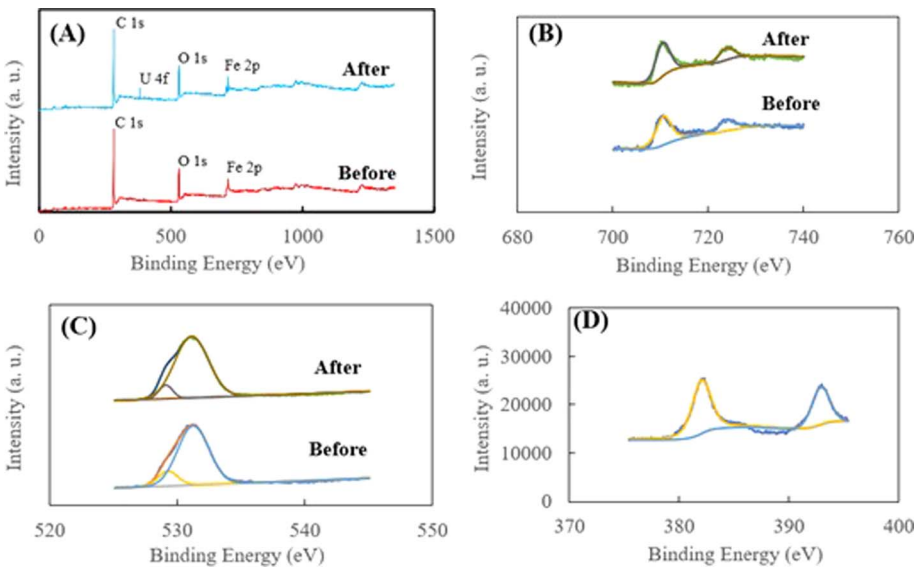

Fig. 6 (A) XPS spectra of HA–Fe_3O_4/BC before and after U(VI) removal; (B) high-resolution XPS spectra of Fe 2p before and after U(VI) removal; (C) high-resolution XPS spectra of O 1s before and after U(VI) removal; and (D) high-resolution XPS spectra of U 4f.

C 1s, O 1s and Fe 2p, respectively. The appearance of Fe 2p implies that the BC nanoparticles were successfully modified by Fe_3O_4 nanoparticles. For HA–Fe_3O_4/BC after the adsorption of U(VI) removal, three peaks of C 1s, O 1s and Fe 2p could be observed. Additionally, the peaks at 382.08 eV could be attributed to U 4f. The appearance of the U 4f peak indicated that U(VI) could be successfully captured on the surface of HA–Fe_3O_4/BC. As illustrated in Fig. 6B, the two peaks at 711.18 and 725.38 eV. They were assigned to Fe $2p_{3/2}$ and Fe $2p_{1/2}$, respectively.[55] This also indicates that Fe_3O_4 nanoparticles appeared on the surface of HA–Fe_3O_4/BC. In addition, the peak areas of Fe $2p_{3/2}$ and Fe $2p_{1/2}$ changed after adsorption of U(VI), which demonstrates that U(VI) could be reduced to U(IV) by Fe^{2+}.

This result is consistent with that illustrated in Fig. 6D. From Fig. 6D, the two peaks at 382.35 and 393.15 eV appeared. They were assigned to U $4f_{5/2}$ and U $4f_{7/2}$, respectively. They could be deconvoluted into U(IV) and U(VI) sub-peaks. This implies that the reduction reaction of U(VI) with Fe_3O_4 nanoparticles occurred on the surface of HA–Fe_3O_4/BC. The O 1s XPS spectra before and after U(VI) removal are shown in Fig. 6C. They could be resolved into two peaks occurring at 531.94 and 534.13 eV, which were ascribed to anionic oxygen and OH^- functional groups on the surface of HA–Fe_3O_4/BC,[56] respectively. The relative proportions of the anionic oxygen and OH^- functional groups decreased after U(VI) removal. They indicated that anionic oxygen and OH^- functional groups played an important

role in the U(VI) removal on the surface of HA–Fe_3O_4/BC. The electrostatic adsorption of anionic oxygen and OH^- functional groups with U(VI) was mainly a reaction process of U(VI) removal onto the HA–Fe_3O_4/BC. Additionally, according to the results of the FT-IR spectra, the number of functional groups (such as –O–H, –C=C–, $-CH_3$ or $-CH_3$, –C–O–C– and Fe–O) could be observed on the surface of HA–Fe_3O_4/BC. They could adsorb U(VI) through inner-sphere surface complexation. Further, the probable mechanism of U(VI) removal by HA–Fe_3O_4/BC is illustrated in Fig. 7. This suggests that the probable mechanism of U(VI) removal by HA–Fe_3O_4/BC could be divided into reduction reaction, inner-sphere surface complexation and electrostatic adsorption.

3.2.4 Recycle experiment and application for real ground water. The reusability of HA–Fe_3O_4/BC was estimated in consecutive cycle experiments. HA–Fe_3O_4/BC after adsorption of U(VI) was soaked with 100 mL of 10% HNO_3 solution for 24 h. The results of recycling experiments are displayed in Fig. 8.

With the increase in the number of cycles, the removal capacity of U(VI) by HA–Fe_3O_4/BC still could reach 110.82 mg g^{-1} after five cycles. This exhibited high stability and reusability.

The real ground water samples contained various background ions. They could impact the performance of the adsorbent for pollutant removal. Therefore, the impact of background cations (Mg^{2+} and Ca^{2+}) and anions (HCO_3^-, and CO_3^{2-}) on HA–Fe_3O_4/BC removal was assessed. As shown in Fig. 9, when each of Mg^{2+}, Ca^{2+}, HCO_3^-, and CO_3^{2-} separately existed in solution, they had an important influence on the U(VI) removal by HA–Fe_3O_4/BC. This might be because adsorption sites on the surface of HA–Fe_3O_4/BC were occupied by background cations and anions (Mg^{2+}, Ca^{2+}, HCO_3^-, and CO_3^{2-}), thus decreasing the adsorption sites.

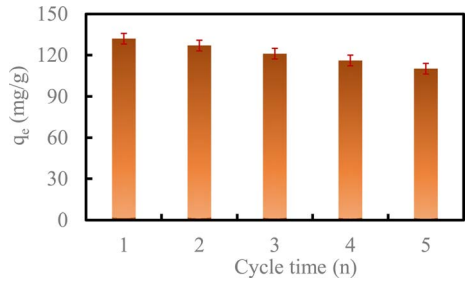

Fig. 8 Regeneration of U(VI) removal by HA–Fe_3O_4/BC (reaction conditions: the dosage of HA–Fe_3O_4/BC was 0.3 g L^{-1}, the reaction time was 300 min, the initial concentration of U(VI) was 50 mg L^{-1}, the temperature was 298 K and the pH in solution was 6.0).

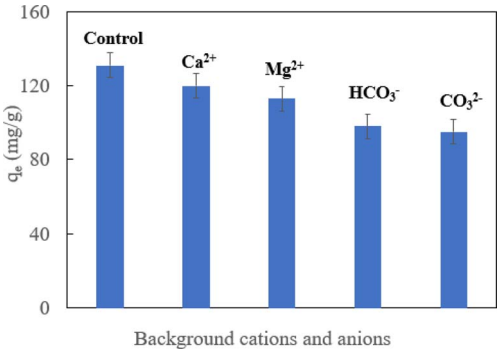

Fig. 9 Background ions on U(VI) removal by HA–Fe_3O_4/BC (reaction conditions: the dosage of HA–Fe_3O_4/BC was 0.3 g L^{-1}, the reaction time was 300 min, the initial concentration of U(VI) was 50 mg L^{-1}, the temperature was 298 K and the pH in solution was 6.0).

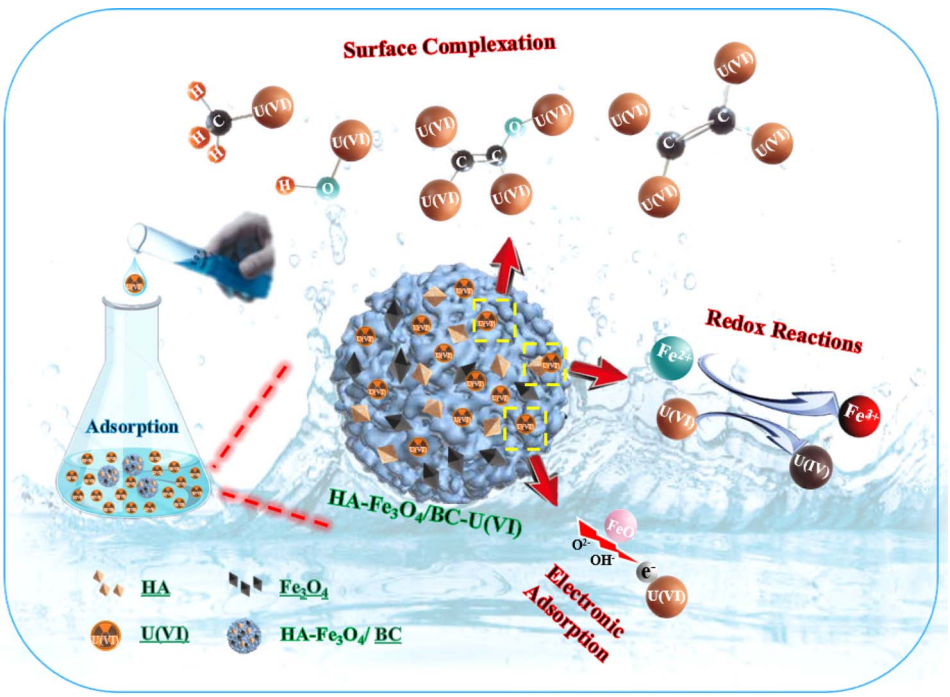

Fig. 7 Proposed mechanism for U(VI) removal by HA–Fe_3O_4/BC.

4 Conclusions

Herein, HA–Fe_3O_4/BC was fabricated using the co-precipitation method to remove U(VI) from the aqueous solution. Adsorption experiments indicated that HA–Fe_3O_4/BC exhibited excellent adsorption performance for U(VI) removal, low cost and wide source. The reaction conditions had an important influence on U(VI) removal by HA–Fe_3O_4/BC. The adsorption processes were dominated by chemisorption and monolayer adsorption. The maximum adsorption capacity of U(VI) by HA–Fe_3O_4/BC could reach 555.56 mg g^{-1}. The probable mechanisms of U(VI) removal by HA–Fe_3O_4/BC were reduction reaction, inner-sphere surface complexation and electrostatic adsorption. It is a promising adsorption material for U(VI) removal.

Data availability

The data and materials presented in this study are available on request from the corresponding author. The data are not publicly available due to privacy restrictions.

Conflicts of interest

There are no conflicts of interest to declare.

Acknowledgements

The authors would like to thank their respective institutes for their support in this research.

References

1 T. Ye, B. Huang, Y. Wang, L. Zhou and Z. Liu, Rapid removal of uranium(VI) using functionalized luffa rattan biochar from aqueous solution, *Colloids Surf., A*, 2020, **606**, 125480.
2 A. Corner, D. Venables, A. Spence, W. Poortinga, C. Demski and N. Pidgeon, Nuclear power, climate change and energy security: exploring British public attitudes, *Energy Policy*, 2011, **39**, 4823–4833.
3 M. Sobczyk, C. Nguyen Dinh, M. Marzec, E. Bazarkina, K. O. Kvashnina, A. Cwanek, E. Lokas and T. Bajda, Insights into uranium sequestration by coal fly-ash-derived zeolites: Understanding *via* wet chemistry, and advanced spectroscopies, *J. Cleaner Prod.*, 2024, **449**, 141206.
4 D. Li and D. I. Kaplan, Sorption coefficients and molecular mechanisms of Pu, U, Np, Am and Tc to Fe (hydr)oxides: a review, *J. Hazard. Mater.*, 2012, **243**, 1–18.
5 A. Gladysz-Plaska, E. Grabias and M. Majdan, Simultaneous adsorption of uranium(VI) and phosphate on red clay, *Prog. Nucl. Energy*, 2018, **104**, 150–159.
6 S. Avasarala, P. C. Lichtner, A. M. S. Ali, R. González-Pinzón, J. M. Blake and J. M. Cerrato, Reactive transport of U and V from abandoned uranium mine wastes, *Environ. Sci. Technol.*, 2017, **51**, 12385–12393.
7 H. Liu, M. Li, T. Chen, C. Chen, N. S. Alharbi, T. Hayat, D. Cheng, Q. Zhang and Y. Sun, New synthesis of nZVI/C composites as an efficient adsorbent for the uptake of U(VI) from aqueous solutions, *Environ. Sci. Technol.*, 2017, **51**, 9227–9234.
8 B. Bajwa, S. Kumar, S. Singh, S. Sahoo and R. Tripathi, Uranium and other heavy toxic elements distribution in the drinking water samples of SW-Punjab, India, *J. Radiat. Res. Appl. Sci.*, 2017, **10**, 13–19.
9 L. Corlin, T. Rock, J. Cordova, M. Woodin, J. L. Durant, D. M. Gute, J. Ingram and D. Brugge, Health effects and environmental justice concerns of exposure to uranium in drinking water, *Curr. Environ. Health Rep.*, 2016, **3**, 434–442.
10 M. Qiu, L. Liu, Q. Ling, Y. Cai, S. Yu, S. Wang, D. Fu, B. Hu and X. Wang, Biochar for the removal of contaminants from soil and water: a review, *Biochar*, 2022, **4**, 19.
11 S. Yu, H. Tang, D. Zhang, S. Wang, M. Qiu, G. Song, D. Fu, B. Hu and X. Wang, MXenes as emerging nanomaterials in water purification and environmental remediation, *Sci. Total Environ.*, 2022, **811**, 152280.
12 A. Elzoghby, H. Fahmy, M. Taha and S. Ibrahim, Active carbon-based waste packaging materials for uranium sorption from aqueous solution, *Environ. Sci. Pollut. Res.*, 2023, **30**, 74726–74741.
13 J. T. Amphlett, M. D. Ogden, R. I. Foster, N. Syna, K. H. Soldenhoff and C. A. Sharrad, The effect of contaminants on the application of polyamine functionalised ion exchange resins for uranium extraction from sulfate based mining process waters, *Chem. Eng. J.*, 2018, **354**, 633–640.
14 K. Kiegiel, A. Abramowska, P. Biełuszka, G. Zakrzewska-Kołtuniewicz and S. Wołkowicz, Solvent extraction of uranium from leach solutions obtained in processing of Polish low-grade ores, *J. Radioanal. Nucl. Chem.*, 2017, **311**, 589–598.
15 M. Chaudhary, L. Singh, P. Rekha, V. C. Srivastava and P. Mohanty, Adsorption of uranium from aqueous solution as well as seawater conditions by nitrogen-enriched nanoporous polytriazine, *Chem. Eng. J.*, 2019, **378**, 122236.
16 T. A. Duster, J. E. S. Szymanowski and J. B. Fein, Experimental measurements and surface complexation modeling of U(VI) adsorption onto multilayered graphene oxide: the importance of adsorbate–adsorbent ratios, *Environ. Sci. Technol.*, 2017, **51**, 8510–8518.
17 J. T. M. Amphlett, M. D. Ogden, R. I. Foster, N. Syna, K. Soldenhoff and C. A. Sharrad, Polyamine functionalised ion exchange resins: synthesis, characterisation and uranyl uptake, *Chem. Eng. J.*, 2018, **334**, 1361–1370.
18 A. Sklodowska, S. Mielnicki and L. Drewniak, Raoultella sp. SM1, a novel ironreducing and uranium-precipitating strain, *Chemosphere*, 2018, **195**, 722–726.
19 T. H. Dao, N. T. Nguyen, M. N. Nguyen, C. L. Ngo, N. H. Luong, D. B. Le and T. D. Pham, Adsorption Behavior of Polyelectrolyte onto Alumina and Application in Ciprofloxacin Removal, *Polymers*, 2020, **12**, 1554.
20 T. Nguyen, Q. Truong, C. Chen, W. Chen and C. Dong, Pyrolysis of marine algae for biochar production for adsorption of Ciprofloxacin from aqueous solutions, *Bioresour. Technol.*, 2022, **351**, 127043.

21 K. Ioannou, P. Hadjiyiannis, I. Liatsou and I. Pashalidis, U(VI) adsorption by biochar fiber-MnO_2 composites, *J. Radioanal. Nucl. Chem.*, 2019, **320**, 425–432.

22 L. Gao, L. Peng, J. Li, W. Zhang and B. Shi, Superefficient separation of Th(IV) and U(VI) by lignin-derived magnetic biochar *via* competitive adsorption mechanism, *Sep. Purif. Technol.*, 2023, **315**, 123635.

23 E. M. Bakhsh, S. B. Khan, K. Akhtar, E. Y. Danish, T. M. Fagieh, C. Qiu, Y. Sun, V. Romanovski and X. Su, Simultaneous preparation of humic acid and mesoporous silica from municipal sludge and their adsorption properties for U(VI), *Colloids Surf., A*, 2022, **647**, 129060.

24 T. Atugoda, C. Gunawardane, M. Ahmad and M. Vithanage, Mechanistic interaction of ciprofloxacin on zeolite modified seaweed (Sargassum crassifolium) derived biochar: Kinetics, isotherm and thermodynamics, *Chemosphere*, 2021, **281**, 130676.

25 S. Bakshi, D. A. Laird, R. G. Smith and R. C. Brown, Capture and Release of Orthophosphate by Fe-Modified Biochars: Mechanisms and Environmental Applications, *ACS Sustain. Chem. Eng.*, 2021, **9**, 658–668.

26 J. He, Y. Xiao, J. Tang, H. Chen and H. Sun, Persulfate activation with sawdust biochar in aqueous solution by enhanced electron donor-transfer effect, *Sci. Total Environ.*, 2019, **690**, 768–777.

27 A. Gopinath, G. Divyapriya, V. Srivastava, A. R. Laiju, P. V. Nidheesh and M. S. Kumar, Conversion of sewage sludge into biochar: A potential resource in water and wastewater treatment, *Environ. Res.*, 2021, **194**, 110656.

28 V. Dhanya and N. Rajesh, A cradle to approach towards remediation of uranium from water using carbonized arecanut hask fiber, *RSC Adv.*, 2023, **13**, 4394–4406.

29 K. M. Poo, E. B. Son, J. S. Chang, X. Ren, Y. J. Choi and K. J. Chae, Biochars derived from wasted marine macroalgae (Saccharina japonica and Sargassum fusiforme) and their potential for heavy metal removal in aqueous solution, *J. Environ. Manage.*, 2018, **206**, 364–372.

30 M. J. Ahmed, P. U. Okoye, E. H. Hummadi and B. H. Hameed, High-performance porous biochar from the pyrolysis of natural and renewable seaweed (Gelidiella acerosa) and its application for the adsorption of methylene blue, *Bioresour. Technol.*, 2019, **278**, 159–164.

31 X. Yao, L. Ji, J. Guo, S. Ge, W. Lu, L. Cai, Y. Wang, W. Song and H. Zhang, Magnetic activated biochar nanocomposites derived from wakame and its application in methylene blue adsorption, *Bioresour. Technol.*, 2020, **302**, 122842.

32 Y. Han, X. Cao, X. Ouyang, S. P. Sohi and J. Chen, Adsorption kinetics of magnetic biochar derived from peanut hull on removal of Cr (VI) from aqueous solution: effects of production conditions and particle size, *Chemosphere*, 2016, **145**, 336–341.

33 K. R. Thines, E. C. Abdullah, N. M. Mubarak and M. Ruthiraan, Synthesis of magnetic biochar from agricultural waste biomass to enhancing route for waste water and polymer application: a review, *Renewable Sustainable Energy Rev.*, 2017, **67**, 257–276.

34 F. Huber, D. Schild, T. Vitova, J. Rothe, R. Kirsch and T. Schafer, U(VI) removal kinetics in presence of synthetic magnetite nanoparticles, *Geochim. Cosmochim. Acta*, 2012, **96**, 154–173.

35 Y. Xie, C. Chen, X. Ren, X. Wang, H. Wang and X. Wang, Emerging natural and tailored materials for uranium-contaminated water treatment and environmental remediation, *Prog. Mater. Sci.*, 2019, **103**, 180–234.

36 X. J. Jin, R. R. Liu, H. F. Wang, L. Han, M. Q. Qiu and B. W. Hu, Functionalized porous nanoscale Fe_3O_4 particles supported biochar from peanut shell for Pb(II) ions removal from landscape wastewater, *Environ. Sci. Pollut. Res.*, 2022, **29**, 37159–37169.

37 Y. Zhang, Y. Li, Y. Ning, D. Liu, P. Tang, Z. Yang, Y. Lu and X. Wang, Adsorption and desorption of uranium (VI) onto humic acids derived from uranium-enriched lignites, *Water Sci. Technol.*, 2018, **77**, 920–930.

38 L. Yao, H. Yang, Z. Chen, M. Qiu, B. Hu and X. Wang, Bismuth oxychloride-based materials for the removal of organic pollutants in wastewater, *Chemosphere*, 2021, **273**, 128576.

39 D. Maity and D. C. Agrawal, Synthesis of iron oxide nanoparticles under oxidizing environment and their stabilization in aqueous and non-aqueous media, *J. Magn. Magn. Mater.*, 2007, **308**, 46–55.

40 W. Li, J. T. Mayo, D. N. Benoit, L. D. Troyer, Z. A. Lewicka, B. J. Lafferty, J. G. Catalano, S. S. Lee, V. L. Colvin and J. D. Fortner, Engineered superparamagnetic iron oxide nanoparticles for ultra-enhanced uranium separation and sensing, *J. Mater. Chem. A*, 2016, **4**, 15022–15029.

41 H. Gonzalez-Raymat, V. Anagnostopoulos, M. Denham, Y. Cai and Y. P. Katsenovich, Unrefined humic substances as a potential low-cost amendment for the management of acidic groundwater contamination, *J. Environ. Manage.*, 2018, **212**, 210–218.

42 S. Yang, P. Zong, X. Ren, Q. Wang and X. Wang, Rapid and highly efficient preconcentration of Eu(III) by core-shell structured Fe_3O_4@humic acid magnetic nanoparticles, *ACS Appl. Mater. Interfaces*, 2012, **4**, 6891–6900.

43 P. Singhal, S. K. Jha, S. P. Pandey and S. Neogy, Rapid extraction of uranium from sea water using Fe_3O_4 and humic acid coated Fe_3O_4 nanoparticles, *J. Hazard. Mater.*, 2017, **335**, 152–161.

44 W. Jiang, Q. Cai, W. Xu, M. Yang, Y. Cai, D. D. Dionysiou, *et al.*, Cr(VI) adsorption and reduction by humic acid coated on magnetite, *Environ. Sci. Technol.*, 2014, **48**, 8078–8085.

45 H. Wang, H. Wang, H. Zhao and Q. Yan, Adsorption and Fenton-like removal of chelated nickel from Zn-Ni alloy electroplating wastewater using activated biochar composite derived from Taihu blue algae, *Chem. Eng. J.*, 2020, **379**, 122372.

46 F. Xiao, J. Cheng, W. Cao, C. Yang, J. Chen and Z. Luo, Removal of heavy metals from aqueous solution using chitosan-combined magnetic biochars, *J. Colloid Interface Sci.*, 2019, **540**, 579–584.

47 D. Cheng, H. H. Ngo, W. Guo, S. W. Chang, D. D. Nguyen, X. Zhang, *et al.*, Feasibility study on a new pomelo peel derived biochar for tetracycline antibiotics removal in swine wastewater, *Sci. Total Environ.*, 2020, **720**, 137662.

48 C. Shan, Z. Ma and M. Tong, Efficient removal of trace antimony(III) through adsorption by hematite modified magnetic nanoparticles, *J. Hazard. Mater.*, 2014, **268**, 229–236.

49 M. Li, H. Liu, T. Chen and W. Lin, Nano-hematite prepared by activation of natural siderite and its performance on immobilization of Eu(III), *Appl. Geochem.*, 2017, **84**, 154–161.

50 C. Ding, W. Cheng, Y. Sun and X. Wang, Effects of Bacillus subtilis on the reduction of U(VI) by nano-Fe^0, *Geochim. Cosmochim. Acta*, 2015, **165**, 86–107.

51 S. Lagergren, Zur theorie der sogenannten adsorption geloster stoffe Pseudo-second order model for sorption processes, *Handlingar*, 1898, **24**, 1–39.

52 H. M. F. Freundlich, Uber die adsorption in lasungen, *J. Phys. Chem.*, 1906, **57**, 385–470.

53 I. Langmuir, The adsorption of gases on plane surface of glass, mica and platinum, *J. Am. Chem. Soc.*, 1918, **40**, 1361–1403.

54 W. S. Hummers and R. E. Offeman, Preparation of graphitic oxide, *J. Am. Chem. Soc.*, 1958, **80**, 1339.

55 C. Galindo, M. Del Nero, R. Barillon, E. Halter and B. Made, Mechanisms of uranyl and phosphate (co)sorption: complexation and precipitation at alpha-Al_2O_3 surfaces, *J. Colloid Interface Sci.*, 2010, **347**, 282–289.

56 C. Ding, W. Cheng, X. Nie and F. Yi, Synergistic mechanism of U(VI) sequestration by magnetite-graphene oxide composites: evidence from spectroscopic and theoretical calculation, *Chem. Eng. J.*, 2017, **324**, 113–121.